

Refractive Indices of Amorphous and Crystalline HNO₃/H₂O Films Representative of Polar Stratospheric Clouds

B. S. Berland, D. R. Haynes,[†] K. L. Foster, M. A. Tolbert,* and S. M. George*

Department of Chemistry and Biochemistry and Cooperative Institute for Research in Environmental Sciences, University of Colorado, Boulder, Colorado 80309

O. B. Toon

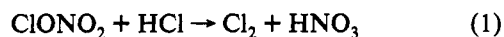
NASA Ames Research Center, Moffett Field, California 94035

Received: November 5, 1993; In Final Form: January 10, 1994*

Optical interference techniques were used to measure the real index of refraction of nitric acid/ice films representative of type I and type II polar stratospheric clouds (PSCs). Possible candidates for type I PSCs include amorphous HNO₃/H₂O mixtures as well as crystalline nitric acid trihydrate (NAT), dihydrate (NAD), and monohydrate (NAM). Amorphous and crystalline model PSC films were grown in vacuum by vapor deposition on single-crystal Al₂O₃ substrates at low temperatures. The real indices of refraction at $\lambda = 632$ nm were measured for these films using the time-dependent optical interference during film deposition. The stoichiometries of the HNO₃/H₂O films were determined using laser-induced thermal desorption (LITD) techniques. For the amorphous films at 130 K, the refractive indices increased with increasing nitric acid content. The values ranged from $n = 1.31 \pm 0.01$ for pure ice to $n = 1.47 \pm 0.01$ for nearly pure nitric acid. A Lorentz-Lorenz analysis was in good agreement with the measured refractive indices of the amorphous HNO₃/H₂O films as a function of HNO₃ mole fraction. Growth of HNO₃/H₂O films at 175 K resulted in the formation of either crystalline NAM or NAD. The crystalline indices were substantially higher than their amorphous analogs. The crystalline refractive indices at 175 K were $n = 1.52 \pm 0.01$ for NAD and $n = 1.54 \pm 0.01$ for NAM. Attempts to measure the refractive index of crystalline NAT were unsuccessful because NAT films would not nucleate under allowable temperature and pressure conditions.

I. Introduction

Heterogeneous reactions on polar stratospheric clouds (PSCs) have been implicated recently in Arctic and Antarctic ozone loss.^{1,2} The most important heterogeneous process on PSCs is thought to be reaction 1. This reaction converts reservoir chlorine



(ClONO₂, HCl) into a photochemically active form (Cl₂). Upon photolysis of Cl₂, chlorine radicals are released to participate in catalytic ozone destruction cycles. Laboratory,³⁻⁹ field,¹⁰⁻¹² and modeling¹³⁻¹⁸ studies have all provided strong evidence supporting the importance of this reaction in polar ozone loss. Although the occurrence of heterogeneous chemistry is well established, there are still uncertainties regarding the chemical composition of the PSCs. Knowledge of the PSC composition is important for predicting both the cloud formation frequency and the rates of subsequent heterogeneous reactions on PSCs.

There are two main types of PSCs.^{19,20} Type II PSCs are solid ice particles that form in the stratosphere at temperatures below ~ 187 K. This low-temperature requirement prevents type II PSCs from forming under most Arctic stratospheric conditions. Type II solid ice clouds are mainly observed in the Antarctic winter and spring and occasionally in the Arctic winter. In contrast, the temperature threshold for type I PSC formation is near 195 K.¹⁹ Consequently, these clouds occur much more frequently in both polar stratospheres and provide more surface area for the occurrence of heterogeneous chemistry. Type I PSCs are thought to be composed of mixtures of nitric acid and water.²⁰⁻²³ More specifically, the particles are currently believed to be either crystalline nitric acid trihydrate (NAT),^{23,24} crystalline

nitric acid dihydrate (NAD),²⁵ or an amorphous HNO₃/H₂O mixture.^{26,27} There are several ongoing field experiments using light scattering techniques to determine the size and composition of type I PSCs.²⁸⁻³¹ However, an accurate knowledge of the refractive indices of HNO₃/H₂O mixtures versus HNO₃ mole fraction is required to identify type I PSCs using these optical techniques.

In this paper, we report measurements of the real index of refraction at $\lambda = 632$ nm for amorphous and crystalline HNO₃/H₂O films using optical interference techniques. The compositions of the HNO₃/H₂O films were accurately determined using laser-induced thermal desorption with mass spectrometric detection. For the amorphous HNO₃/H₂O films, the refractive indices were measured for a wide range of HNO₃ mole fractions from pure water to nearly pure nitric acid. For the crystalline hydrates, refractive indices were measured for nitric acid monohydrate (NAM) and nitric acid dihydrate (NAD). The refractive index for crystalline nitric acid trihydrate (NAT) could not be determined because NAT did not form under the temperature and pressure conditions allowed by our experiments.

II. Experimental Section

A. Vacuum Chamber and Al₂O₃ Substrate. The experimental apparatus used to measure the refractive indices is shown in Figure 1. Briefly, a single-crystal Al₂O₃(0001) substrate was positioned at the bottom of a cryostat in an ultrahigh vacuum chamber.^{32,33} This chamber was pumped by tandem turbomolecular pumps to a base pressure of 5×10^{-10} Torr. The chamber was equipped with a quadrupole mass spectrometer (UTI 100C) for the laser-induced thermal desorption (LITD) measurements and residual gas analysis. Two independently controlled leak valves allowed the H₂O and HNO₃ vapors to be introduced into the chamber.

The Al₂O₃ crystal, obtained from Insaco Inc., had dimensions of 21 mm \times 12 mm \times 0.5 mm. This Al₂O₃(0001) substrate was

[†] Present address: Weyerhaeuser Technology Center, Tacoma, WA 98477.

* Abstract published in *Advance ACS Abstracts*, March 15, 1994.

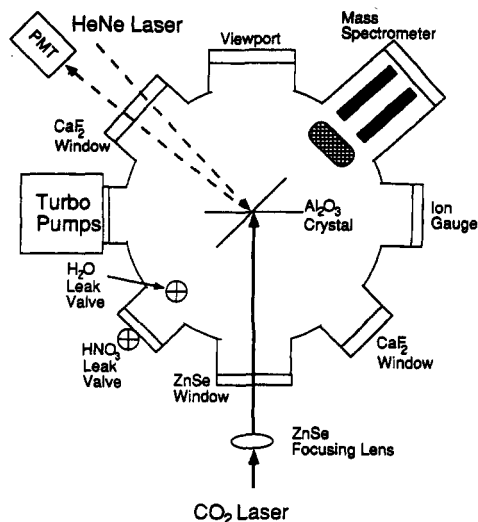


Figure 1. Schematic of the experimental setup. The two solid lines for the Al₂O₃ crystal represent the positions for interference and LITD measurements.

mounted to the cryostat and cleaned in vacuum using techniques described earlier.³² A thin coating of tantalum sputtered on the back side of the substrate allowed resistive heating. In conjunction with liquid nitrogen cooling, a wide range of temperatures could easily be obtained from 90 to 500 K.

B. Film Preparation. The films were prepared by backfilling both H₂O and HNO₃ onto the Al₂O₃(0001) surface at 130 K. H₂O vapor was taken above a reservoir of deionized, distilled water. HNO₃ was prepared by combining commercial 70 wt % nitric acid and 96 wt % sulfuric acid in a 1:3 volume ratio. The vapor over this mixture is >95% by mass HNO₃ and contains only a small contribution from H₂O.³⁴ The H₂O and HNO₃ samples were both purified by several freeze-pump-thaw cycles using liquid nitrogen.

The partial pressures of the HNO₃ and H₂O gases were monitored with the quadrupole mass spectrometer. Mass 46 was used to measure HNO₃ and mass 18 to measure H₂O. The actual pressures of these species were typically ~10⁻⁷ Torr for HNO₃ and ~10⁻⁶–10⁻⁵ Torr for H₂O. Amorphous films were grown by codepositing water and nitric acid onto the cooled Al₂O₃ substrate at 130 K. Similar pressures of HNO₃ were used for all of the amorphous films. Varying H₂O pressures were employed to obtain the desired HNO₃/H₂O stoichiometry. Crystalline NAM and NAD films were prepared with the Al₂O₃ substrate at 175 K. These films were assumed to be crystalline because previous infrared spectroscopic studies have shown that crystalline films will grow at 175 K rather than amorphous films.^{35,36} NAM and NAD films could easily be prepared by direct deposition of the HNO₃/H₂O vapors onto Al₂O₃(0001) at 175 K.

After the amorphous or crystalline film growth, the HNO₃ and H₂O gas inlets were closed to reduce the pressures of these gases. Subsequently, the surface temperature was immediately lowered to 90 K. This lower temperature prevented HNO₃/H₂O film evaporation that is negligible at 130 K but is measurable near 175 K. The LITD measurements were then performed with the Al₂O₃ substrate at 90 K to obtain the HNO₃/H₂O film stoichiometry.

Crystalline NAT would *not* readily nucleate on the Al₂O₃ substrate under the allowable temperature and pressure regimes of our vacuum apparatus. At 175 K, the stability region for NAT is very small, and only a small range of HNO₃ and H₂O pressures should form NAT.²⁵ At a warmer temperature of 180 K, the stability region is more extensive. However, every attempt to grow NAT directly on the Al₂O₃ substrate at 175–180 K resulted in the formation of either NAD or ice. This behavior is in qualitative agreement with the observation by Worsnop et

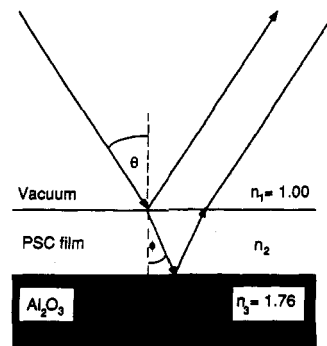


Figure 2. Schematic representation of the geometry for optical interference measurements. The solid line shows the He-Ne laser path.

al.²⁵ that NAT does not readily nucleate on glass but requires a layer of ice for nucleation and growth.

Temperatures higher than 180 K could not be utilized to grow NAT because small thermal gradients across the Al₂O₃ crystal led to extremely nonuniform films. These films could vary in composition by as much as a factor of 20 across the crystal. This nonuniformity may reflect the rapid evaporation rates from ice or HNO₃/H₂O surfaces at temperatures greater than 180 K.³⁷ Consequently, a thermal gradient of only a few degrees can have a large effect on the film growth rates.

Nucleation of NAT on thin ice films was also unsuccessful. For these experiments, the crystal mount was modified to produce fairly uniform films at higher temperatures up to 200 K. The NAT stability region at these higher temperatures is larger and NAT should grow readily.²⁵ To nucleate NAT on the thin ice films, the H₂O pressure was increased to the ice frost point, and an ice film of ~300–400 Å was deposited on the Al₂O₃ substrate as monitored by optical interference. The H₂O pressure was then lowered to just below the frost point and the ice film was allowed to desorb slowly. The HNO₃ pressure was then increased until a HNO₃/H₂O film began to grow on top of the ~300-Å-thick ice film.

Growth of these films was extremely slow and some films required up to 3 h to grow ~1000 Å. The LITD determination of the film composition was complicated by the underlying ice layer. However, LITD analysis revealed that most of the films were 1:2 or 1:1 HNO₃:H₂O before subtracting the contribution from the ice film. Another difficulty with the LITD analysis was that sample cooling from 200 K to temperatures below 160 K where desorption is negligible required several minutes. Consequently, HNO₃ and H₂O desorption during cooling could have affected the film content and prevented an accurate LITD determination of the film composition. Attempts to increase the H₂O concentration of the films resulted in mostly ice films. A few films were consistent with higher hydrates with compositions around 1:6–8 HNO₃:H₂O. Unfortunately, no films were consistent with a crystalline NAT composition.

C. Optical Interference Measurements. The film thickness was monitored by the optical interference of a reflected helium-neon laser at $\lambda = 632$ nm as shown schematically in Figure 2.³⁷ The He-Ne laser was incident on the growing model PSC film at near normal incidence. The resulting reflections from the vacuum-film and film-Al₂O₃ interfaces led to constructive and destructive interference in the reflected laser beam. This reflectance was monitored with a Hamamatsu R928 photomultiplier tube.

The thickness of the film, x , was derived from the optical interference using the equation

$$x = \frac{m\lambda}{2n(T)} \quad (2)$$

In this equation, $\lambda = 632$ nm, m is the number of periods of oscillation, and $n(T)$ is the temperature-dependent real refractive

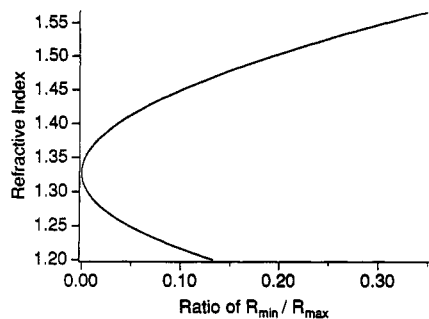


Figure 3. Refractive index of the PSC film, n_2 , determined from eq 5 as a function of the He-Ne laser reflectance ratio, R_{\min}/R_{\max} .

index of the film. Given typical refractive indices of $n = 1.31$ – 1.47 , thicknesses of $x \approx 1210$ – 1080 Å correspond to half-cycles of oscillation between maxima and minima.

Optical interference was also used to measure the real indices of refraction of the amorphous and crystalline $\text{HNO}_3/\text{H}_2\text{O}$ films. From Fresnel's equations,³⁸ the theoretical reflectance at normal incidence can be shown to be a function of n_1 , n_2 , and n_3 , which are the refractive indices of vacuum (n_1), the PSC film (n_2), and the Al_2O_3 crystal (n_3). When $n_3 > n_2 > n_1$, the maximum reflectance, R_{\max} , and minimum reflectance, R_{\min} , occurring during constructive and destructive interference are³⁸

$$R_{\max} = \left[\frac{n_1 - n_3}{n_1 + n_3} \right]^2 \quad (3)$$

$$R_{\min} = \left[\frac{n_1 n_3 - n_2^2}{n_1 n_3 + n_2^2} \right]^2 \quad (4)$$

These two equations for R_{\max} and R_{\min} can be combined to obtain

$$\frac{R_{\min}}{R_{\max}} = \frac{\left[\frac{n_1 n_3 - n_2^2}{n_1 n_3 + n_2^2} \right]^2}{\left[\frac{n_1 - n_3}{n_1 + n_3} \right]^2} \quad (5)$$

The ratio R_{\min}/R_{\max} can be experimentally determined by measuring the reflectance versus film thickness. The refractive index of vacuum is $n_1 = 1.0$ and the refractive index of Al_2O_3 is $n_3 = 1.76$.^{39,40} Consequently, the index of refraction of the PSC film, n_2 , can be determined using eq 5. A plot of the dependence of n_2 on the ratio R_{\min}/R_{\max} is shown in Figure 3. This figure illustrates that two values of n_2 correspond to each R_{\min}/R_{\max} ratio. However, only one of the two n_2 values will be physically reasonable for $R_{\min}/R_{\max} > 0.01$.

This optical interference analysis can be extended to multilayered systems. Recursion relations for the reflectance from an n -layer system have been presented earlier.⁴¹ The equations for a two-layer system are described in detail.⁴² These equations could have been used for the analysis of NAT growth if NAT nucleation on the thin ice films had been successful.

D. LITD Film Composition Measurements. The $\text{HNO}_3/\text{H}_2\text{O}$ film composition was determined using laser-induced thermal desorption (LITD) techniques.^{43–45} For a typical LITD measurement, a short laser pulse is focused onto a surface. Absorption of light by the substrate and the adlayer leads to the rapid localized heating of the illuminated area. This heating promotes the thermal desorption of the surface species. The desorbed species then rapidly equilibrate in the vacuum chamber and are monitored with a mass spectrometer.

A Lumonics pulsed CO_2 transversely excited atmospheric (TEA) laser at $\lambda = 10.6$ μm was used for these LITD measurements. The TEA CO_2 laser was modified to produce a TEM-00 laser beam using a 10-mm-diameter intracavity aperture

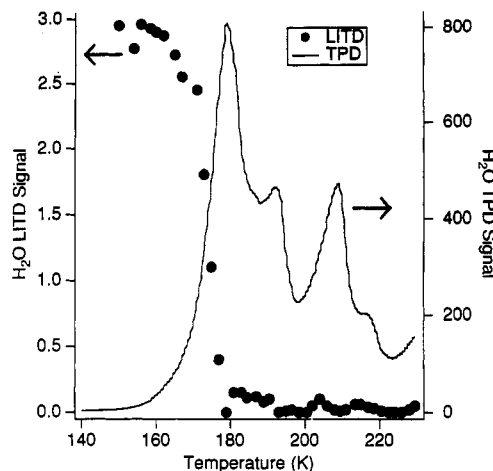


Figure 4. Comparison of the LITD and TPD methods of analysis for a pure ice film on $\text{Al}_2\text{O}_3(0001)$. Extra TPD peaks at higher temperatures are not derived from the Al_2O_3 surface.

in contact with the output mirror.⁴⁶ The resultant CO_2 laser beam had a Gaussian spatial distribution, a pulse duration of ~ 100 ns (fwhm), and an energy of ~ 10 mJ/pulse.⁴⁶ The CO_2 laser beam was focused onto the $\text{Al}_2\text{O}_3(0001)$ surface using an $f = 75$ cm focal length ZnSe lens. The focused spot on the Al_2O_3 surface was ~ 1 mm in diameter.

The 10.6 - μm radiation was absorbed by two phonon transitions in Al_2O_3 .⁴⁷ The optical penetration depth was $1/\alpha \approx 65$ μm for $\text{Al}_2\text{O}_3(0001)$ with the incident light polarized perpendicular to the c -axis of the Al_2O_3 crystal.⁴⁷ The 10.6 - μm radiation was also absorbed by molecular librations in ice with a penetration depth of $1/\alpha \approx 8$ μm .^{48,49} Films containing HNO_3 had an additional absorption of the CO_2 laser light.^{35,49} The approximate penetration depth could be as small as $1/\alpha \approx 2$ μm for some of the amorphous NAM films.

The temperature-programmed LITD (TP-LITD) measurements^{44,45,50} for a pure ice film on $\text{Al}_2\text{O}_3(0001)$ are shown in Figure 4. As the ice film is heated at 2 K/s, the CO_2 laser is directed sequentially onto neighboring spots on the Al_2O_3 substrate. The desorbed flux from each laser shot is proportional to the ice coverage at that time. This desorbed flux is plotted as a function of temperature during the heating ramp in Figure 4. A decrease in the H_2O surface coverage at 175–180 K is observed during the TP-LITD measurements.

The technique of temperature-programmed desorption (TPD) could also be used to determine film compositions.³⁶ In TPD, a surface is resistively heated to cause the thermal desorption of the adsorbed species. The desorption flux is then recorded with a mass spectrometer to determine the composition of the desorbing gases. A TPD curve at 2 K/s for the evaporation of a pure ice film is also shown in Figure 4. In contrast to the single decrease in the H_2O coverage on the Al_2O_3 surface measured using LITD, the TPD measurement displays several H_2O peaks.

A comparison of the LITD and TPD measurements illustrates the advantages of the LITD film composition measurements. The multiple H_2O TPD peaks do *not* all correspond to H_2O desorption from the Al_2O_3 surface. Whereas LITD employs a rapid localized heating of only the adlayer and the Al_2O_3 surface, the resistive heating of the Al_2O_3 substrate indirectly heats a number of other surfaces including the cryostat and mounting assembly. Consequently, the TPD analysis records the H_2O desorption from all of these surfaces. The TP-LITD measurements reveal that only the low-temperature TPD peak at ~ 175 K corresponds to H_2O desorption from the Al_2O_3 surface. As a result of the ambiguities of the TPD analysis, only the LITD technique was used to obtain $\text{HNO}_3/\text{H}_2\text{O}$ film stoichiometries.

Prior to the LITD measurements of the $\text{HNO}_3/\text{H}_2\text{O}$ film stoichiometry, the LITD mass spectrometer signals were cali-

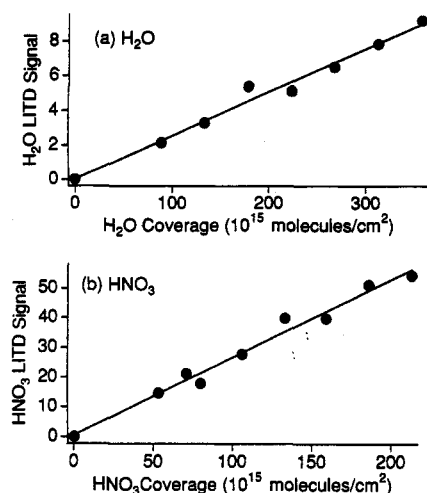


Figure 5. Calibrations of the LITD signal versus surface coverage for (a) H₂O and (b) HNO₃ films.

brated using pure films of H₂O and HNO₃. A film of pure crystalline ice was initially prepared at 130 K, and the film thickness was determined by optical interference as described in section IIC. This thickness was then converted to a H₂O coverage (molecules/cm²) using the density of pure ice, $\rho = 0.93 \text{ g/cm}^3$.⁴⁸ The ice film was then cooled to 90 K, and LITD measurements at mass 18 were recorded with the quadrupole mass spectrometer. Figure 5a shows the LITD signals as a function of H₂O coverage for pure crystalline ice on Al₂O₃(0001) at 90 K. There is a linear relationship between the H₂O coverage and the H₂O LITD signals over the entire coverage range. A two-point calibration of H₂O LITD signal versus H₂O coverage was performed at the beginning of each day to check for possible drift in the quadrupole mass spectrometer.

A similar calibration of the HNO₃ LITD signals was accomplished using mass 46. The HNO₃ calibration was complicated by the small amounts of H₂O in the HNO₃ films. This residual H₂O resulted from the contribution of H₂O to the vapor pressure over the nitric acid/sulfuric acid solution.³⁴ The H₂O fraction was measured by the LITD analysis and subtracted from the total film thickness using the H₂O calibrations. This procedure allowed the determination of the actual HNO₃ film thickness. This corrected HNO₃ thickness was then converted to a HNO₃ coverage using the density of crystalline HNO₃, $\rho = 1.88 \text{ g/cm}^3$.⁵¹ Figure 5b shows that the HNO₃ LITD signal is linear with HNO₃ coverage for all coverages. A two-point calibration of the HNO₃ LITD signal versus HNO₃ coverage was also conducted daily.

Based on the calibrations in Figure 5, LITD measurements were used to obtain the composition of the model PSC films. The amorphous and crystalline model PSC films were prepared as described in section IIB. After the HNO₃/H₂O films were deposited, the films were cooled to 90 K and the H₂O and HNO₃ coverages were determined using LITD measurements. With quadrupole mass spectrometry detection, each CO₂ laser pulse could measure the localized surface coverage of either H₂O or HNO₃. Sixteen separate positions on the Al₂O₃ crystal could be examined with the $\sim 1\text{-mm}$ -diameter desorption area produced by the CO₂ laser. Half of these positions were used to measure the H₂O coverage and the other half were used for the HNO₃ coverage. The results showed that the LITD signals were uniform to $\pm 15\%$ across the Al₂O₃(0001) surface, and the average measured HNO₃ and H₂O coverage was used to determine the HNO₃/H₂O film stoichiometry.

III. Results and Discussion

A. Refractive Indices of Pure Ice and Nitric Acid. The index of refraction of pure ice was first measured to verify this experimental approach. A typical optical interference pattern for pure H₂O ice grown at 130 K is shown in Figure 6a. At a

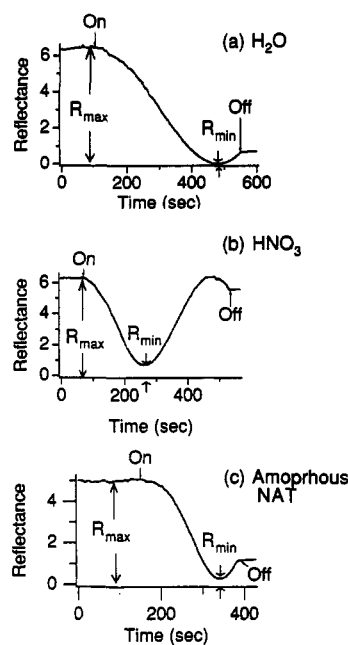


Figure 6. Typical optical interference data for refractive index measurements. The time-dependent He-Ne laser reflectance is shown for (a) ice, (b) HNO₃, and (c) amorphous NAT. Film growth was initiated by opening leak valves (on) and terminated by closing the leak valves (off).

time of ~ 100 s, the H₂O valve was opened to the vacuum chamber and H₂O began to condense on the Al₂O₃ substrate. The ice growth was accompanied by changes in the reflectance of the He-Ne laser. The valve was closed and ice growth stopped at a time of ~ 550 s. The flat line after 550 s indicates that the ice film was stable at 130 K, as expected given the H₂O desorption kinetics from ice.³⁷

The value of $R_{\text{max}} = 6.5$ was determined from the average of the reflectance data between 0 and 100 s. The value of $R_{\text{min}} = 0.01$ was obtained from the average of ~ 10 points at the minimum near 485 s. With these values for R_{min} and R_{max} , eq 5 gives two possible solutions for the index of refraction for pure ice: $n = 1.31$ or $n = 1.34$. The value of $n = 1.31$ was chosen for its excellent agreement with the accepted value of $n = 1.31$ at 266 K.⁵² The measured index of refraction of ice was highly reproducible and was checked on a daily basis in conjunction with the LITD calibrations. All measured values for the refractive index of ice were $n = 1.31 \pm 0.01$.

The problem of the two possible solutions for the refractive index only affected the HNO₃/H₂O films with the lowest HNO₃ mole fractions. For the measurements at higher HNO₃ mole fractions, the second possible value of the refractive index was significantly less than the refractive index of pure ice and was easily eliminated. Due to the low value of R_{min} for ice, determination of its real refractive index is a stringent test on the accuracy of the other higher refractive indices which correspond to larger R_{min} values.

The index of refraction of ice was also measured at 90 K. At this lower temperature, the measured index of refraction was $n = 1.27$. This refractive index is significantly lower than the index of $n = 1.31$ obtained at 130 K. This lowering in the refractive index can be explained by the formation of a microporous ice. Microporous ice has been shown to form at temperatures ≤ 90 K.⁵³ This ice has a large surface area on the order of $\sim 400 \text{ m}^2/\text{g}$ with pore diameters $< 2 \text{ nm}$.⁵⁴ The pores have been shown to collapse at temperatures above 120 K to form more dense, cubic ice.^{53,54} The lower refractive index for ice at 90 K is attributed to the lower bulk density of microporous ice; e.g., $\rho = 0.81 \text{ g/cm}^3$ at 82 K.⁵⁵ Our value for the refractive index of ice at 90 K, $n = 1.27$, is in excellent agreement with the index of $n = 1.275$ reported for amorphous ice at $\lambda = 400 \text{ nm}$ and 77 K.⁵⁶

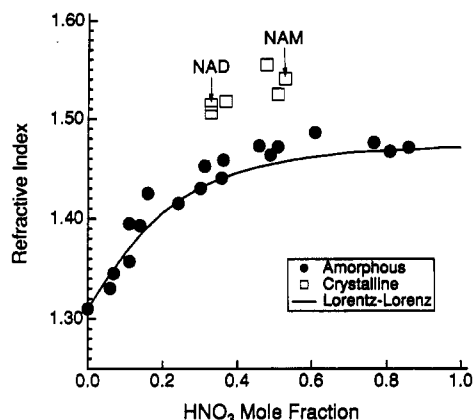


Figure 7. Refractive index versus HNO₃ mole fraction for amorphous and crystalline model PSC films. Amorphous films were prepared at 130 K and crystalline films at 175 K. The solid line shows the prediction of the Lorentz-Lorenz additivity analysis.

TABLE 1: Refractive Indices for Ice and HNO₃/H₂O Films

	amorphous	crystalline
NAM	1.47 ^a	1.54 ^b
NAD	1.45 ^a	1.51 ^b
NAT	1.43 ^a	
ice	1.27 ^c	1.31 ^a

^{a-c} The refractive indices were measured at $\lambda = 632$ nm and at temperatures of (a) 130 K for the ice and amorphous HNO₃/H₂O films, (b) 175 K for the crystalline HNO₃/H₂O films, and (c) 90 K for microporous (amorphous) ice.

In other experiments at 130 K, thicker ice films were grown to observe multiple interference maxima and minima. These maxima and minima did not change as a function of film thickness. This behavior indicates that the ice films were optically flat. If the ice films were heterogeneous or granular, the inhomogeneous film could not produce the nearly 100% reflectance modulation observed in Figure 6a. Likewise, light scattering would progressively attenuate the reflectance, and reproducible maxima and minima would not be observed. The agreement between the measured refractive indices and literature values also argues that the ice films are optically flat.

The refractive index of nearly pure HNO₃ was also measured at 130 K. A typical interference pattern for a growing HNO₃ film is displayed in Figure 6b. R_{\min} is observed at ~ 270 s for the maximum destructive interference. R_{\max} returns to its original value at ~ 460 s for maximum constructive interference during film growth. From the ratio R_{\min}/R_{\max} , the refractive index of this HNO₃ film was $n = 1.47$. Although no values are available at 130 K, previous studies have reported a refractive index for pure HNO₃ of $n = 1.40$ at 278 K.⁵¹ A recent estimate for the refractive index at 158 K yielded a value of $n = 1.48$ based on the temperature dependence of the HNO₃ density.³⁶ This estimate assumed that there are no discontinuities in the refractive index between the liquid and solid phases. The refractive index of HNO₃ was measured daily and was highly reproducible.

B. Refractive Indices of Nitric Acid/Ice Mixtures. The refractive indices were also measured for the amorphous and crystalline nitric acid/ice films. Figure 6c shows the interference pattern for an amorphous HNO₃/H₂O film grown at 130 K. The LITD measurements for this film revealed a stoichiometry of 1:2.9 HNO₃:H₂O. The refractive index obtained from the ratio of R_{\min}/R_{\max} was $n = 1.42$. This index is intermediate between the indices of pure H₂O and nearly pure HNO₃. Figure 7 shows the refractive indices for a series of amorphous and crystalline HNO₃/H₂O films versus the HNO₃ mole fraction. The data for amorphous and crystalline NAM (1:1) and NAD (1:2) and amorphous NAT (1:3) films are summarized in Table 1.

Figure 7 reveals that the refractive index for the amorphous HNO₃/H₂O films increases smoothly from $n = 1.31$ to $n = 1.47$

as the film composition varies from pure ice to nearly pure HNO₃. The refractive index leveled off near $n = 1.47$ for HNO₃ mole fractions greater than 0.5. The approximate reproducibility of most of the amorphous refractive indices was $\Delta n = \pm 0.01$. Films with lower HNO₃ mole fractions had a larger uncertainty of approximately $\Delta n = \pm 0.02$. These larger errors at lower HNO₃ mole fraction are attributed to larger uncertainties in the HNO₃/H₂O film composition caused by smaller HNO₃ LITD signals.

Figure 7 also displays a Lorentz-Lorenz additivity analysis for the refractive indices of the amorphous mixtures. The Lorentz-Lorenz analysis assumes that the polarizability of a composite film is simply the sum of the polarizabilities of the constituents.⁵⁷ This analysis has previously been shown to model the measured refractive indices of liquid H₂SO₄/H₂O mixtures at 288 K.³⁸ The Lorentz-Lorenz additivity analysis determines the refractive index of a mixture from the individual molar refractivities, A , of the components. The molar refractivity for a single constituent is defined as³⁸

$$A = \frac{w(n^2 - 1)}{\rho(n^2 + 2)} \quad (6)$$

In this expression, w is the molecular weight and ρ is the density. The Lorentz-Lorenz analysis assumes that the molar refractivities of the components are additive.^{38,57} Consequently, the molar refractivity of a two-component film is given by

$$A_{\text{film}} = \chi_{\text{H}_2\text{O}} A_{\text{H}_2\text{O}} + \chi_{\text{HNO}_3} A_{\text{HNO}_3} = \frac{w_a(n^2 - 1)}{\rho_a(n^2 + 2)} \quad (7)$$

where χ is the mole fraction of H₂O or HNO₃. Likewise, w_a is the average molecular weight of the film and ρ_a is the average density of the film.

The refractive indices for HNO₃/H₂O films as a function of HNO₃ mole fraction were calculated using eqs 6 and 7. $A_{\text{H}_2\text{O}} = 3.5$ cm³/mol was calculated using eq 6 for H₂O with $\rho = 1.0$ g/cm³, $w = 18$ g/mol and $n = 1.31$. $A_{\text{HNO}_3} = 11.5$ cm³/mol was calculated for HNO₃ with $\rho = 1.54$ g/cm³, $w = 63$ g/mol, and $n = 1.47$. Liquid densities at 278 K for HNO₃/H₂O solutions as a function of HNO₃ mole fraction⁵⁸ were used because the densities of the low-temperature HNO₃/H₂O amorphous solids are not known. The Lorentz-Lorenz analysis is shown as the solid line in Figure 7.

The simple Lorentz-Lorenz additivity model describes the refractive indices of the amorphous HNO₃/H₂O films extremely well. The Lorentz-Lorenz analysis is in agreement even though the chemical nature of the film is changing versus HNO₃ mole fraction. For example, molecular HNO₃ is the main constituent in amorphous 1:1 HNO₃:H₂O, whereas the NO₃⁻ ion dominates in films more dilute than 1:3 HNO₃:H₂O.³⁵ The fact that the simple Lorentz-Lorenz analysis fits the data well suggests that the polarizability is dominated by the individual atoms in the film.

For each of the crystalline films studied, the index of refraction was considerably larger than for its amorphous analog. The estimated reproducibility of these crystalline indices was $\Delta n = \pm 0.01$. The higher refractive indices for the crystalline NAM and NAD films may simply correspond to the larger densities of the crystalline hydrates. The density of NAM is $\rho = 1.82$ g/cm³ at 78 K⁶⁰ compared with a density of $\rho = 1.47$ g/cm³ for a 1:1 HNO₃:H₂O liquid solution at 278 K.⁵⁸ The crystalline densities are also larger than the amorphous densities predicted from the temperature dependence of liquid solutions.⁵⁸

The Lorentz-Lorenz additivity analysis can also be used to predict the refractive indices of the crystalline hydrate films. This analysis assumes that the differences between the amorphous and crystalline films can be ascribed to only changes in density. The Lorentz-Lorenz analysis ignores any possible collective or

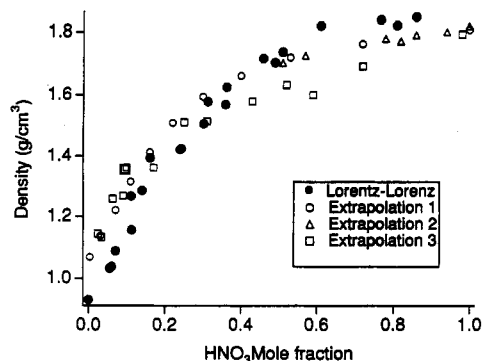


Figure 8. Density of the amorphous HNO₃/H₂O films versus HNO₃ mole fraction. The solid circles represent the values calculated from the measured refractive indices at 130 K using the Lorentz–Lorenz relations. Open symbols are values extrapolated from density versus temperature data: extrapolation 1 (ref 58); extrapolation 2 (ref 61, Veley and Manley); extrapolation 3 (ref 61, Chanukvadze).

ordering effects in the crystal. With densities of $\rho = 1.62 \text{ g/cm}^3$ for NAT at 85 K,⁵⁹ $\rho = 1.82 \text{ g/cm}^3$ for NAM at 78 K,⁶⁰ and $\rho = 1.78 \text{ g/cm}^3$ for NAM at 225 K,⁶⁰ the Lorentz–Lorenz model predicts refractive indices of $n = 1.52$ for NAT and $n = 1.59$ at 78 K or $n = 1.57$ at 225 K for NAM.

The Lorentz–Lorenz refractive index for NAM is slightly larger than the measured value. If the Lorentz–Lorenz model is appropriate, this slight disagreement might suggest a change in the molar refractivity in going from the amorphous films to crystalline solids. Using eq 6 with $n = 1.54$ and $\rho = 1.78 \text{ g/cm}^3$ yields a molar refractivity of $7.1 \text{ cm}^3/\text{mol}$ for NAM. In comparison, the Lorentz–Lorenz relations in eq 7 yield $7.5 \text{ cm}^3/\text{mol}$. Although the Lorentz–Lorenz predictions may not be extremely accurate for the crystalline lattices, the general agreement between the experimental and calculated refractive index for NAM suggests that the higher refractive indices for the crystalline hydrates correlate with their larger densities.

C. Densities of Amorphous Nitric Acid/Ice Mixtures. In the above Lorentz–Lorenz analysis of the refractive index, literature values were used for the densities of the amorphous films. However, the only available data for density versus HNO₃ mole fraction were for liquid solutions at 278 K.⁵⁸ Our experimental refractive indices and the Lorentz–Lorenz relations can be used to estimate the density of the amorphous HNO₃/H₂O films at 130 K. For these estimates, density end points for ice at 143 K and solid HNO₃ at 78 K were employed because they should more closely approximate the solid densities at 130 K than would the liquid densities at 278 K.

$A_{\text{H}_2\text{O}} = 3.73 \text{ cm}^3/\text{mol}$ was calculated using eq 6 for ice I_c with $\rho = 0.93 \text{ g/cm}^3$, $w = 18 \text{ g/mol}$, and $n = 1.31$. $A_{\text{HNO}_3} = 9.35 \text{ cm}^3/\text{mol}$ was calculated for solid HNO₃ with $\rho = 1.88 \text{ g/cm}^3$, $w = 63 \text{ g/mol}$, and $n = 1.47$. Molar refractivities for the HNO₃/H₂O films were calculated from eq 7 using the mole fractions of H₂O and HNO₃ determined by the LITD measurements. Subsequently, the film densities were calculated versus HNO₃ mole fraction from eq 7 using the measured refractive indices.

The densities of the amorphous films versus HNO₃ mole fraction are shown in Figure 8. These calculated values are compared with extrapolations based on literature values. The literature values were extrapolated to 130 K using a linear fit of data obtained at temperatures greater than 273 K.^{58,61} For HNO₃ mole fractions greater than 0.1, the density versus temperature plots were linear. However, at HNO₃ mole fractions less than 0.1, the density versus temperature relationships were not strictly linear, and thus the extrapolations should be upper limits to the true values. The extrapolated densities and the densities from the Lorentz–Lorenz analysis are in good agreement.

D. Atmospheric Implications. At least two groups have tried to determine the composition of polar stratospheric clouds by

measuring the real refractive index of cloud particles. Rosen *et al.* first optically measured the particle size distribution and then measured the particle backscatter on two Arctic balloon flights separated by 6 h.²⁹ The refractive indices were determined by calculating the expected backscatter using the measured size distribution and assuming the particles were spherical. The principal source of error in this determination was that the particle sizes were not measured above $1.8 \mu\text{m}$, although the mean particle size was probably greater than $2.0 \mu\text{m}$.²⁹

Due to the inherent uncertainty in the measurements, the real index at $\lambda = 940 \text{ nm}$ was stated to be between $n = 1.4$ and $n = 1.5$.²⁹ The refractive index should not vary by more than $\Delta n = 0.02$ between our measurements at $\lambda = 632 \text{ nm}$ and Rosen's measurement at $\lambda = 940 \text{ nm}$. These measurements are consistent with our measured refractive indices but are not precise enough to make a compositional identification.

Deshler *et al.* made balloon-borne optical measurements of the PSC size distribution.³⁰ From these measurements, Mie theory was used to calculate lidar backscatter cross sections for comparison with nearly simultaneous ground-based lidar measurements. Most of the lidar data were found to require a real refractive index of about $n = 1.5$. Our measured refractive indices suggest that these data are consistent with PSCs composed of crystalline compounds. However, Deshler *et al.* observed one case in which the lidar data required a real index of about $n = 1.37$. According to our data, this lower refractive index requires a HNO₃/H₂O compound that is amorphous with slightly more H₂O than amorphous NAT.

Refractive indices obtained by optical scattering measurements provide a noninvasive and *in situ* means to confirm the composition of PSCs. Because the refractive index is a macroscopic property, the measured refractive indices cannot definitively establish the individual constituents in PSCs. Other molecules, such as sulfuric acid, may also be present,⁶² and these additional constituents would prevent a unique mapping between the refractive index and the order and composition of the PSCs. However, if the PSC is known to be composed of only HNO₃ and H₂O by other methods, the refractive indices shown in Figure 7 can be used to establish the PSC structure and HNO₃ mole fraction.

IV. Conclusions

The refractive indices of amorphous and crystalline HNO₃/H₂O films on Al₂O₃(0001) were measured using optical interference techniques. The maximum and minimum reflectance during film deposition allowed the refractive indices at $\lambda = 632 \text{ nm}$ to be determined using Fresnel's equations. The composition of the deposited HNO₃/H₂O films was established using laser-induced thermal desorption (LITD) techniques. For the amorphous HNO₃/H₂O films at 130 K, the refractive indices versus HNO₃ mole fraction increased from $n = 1.31 \pm 0.01$ for pure ice to $n = 1.47 \pm 0.01$ for nearly pure nitric acid. The refractive indices versus HNO₃ mole fraction were modeled extremely well by a Lorentz–Lorenz analysis. The crystalline hydrates at 175 K displayed refractive indices that were significantly larger than the amorphous films. The crystalline refractive indices were $n = 1.52 \pm 0.01$ for NAD and $n = 1.54 \pm 0.01$ for NAM. The higher indices for the crystalline hydrates may simply reflect their larger densities.

Acknowledgment. This research was supported by grants from the Office of Naval Research (N00014-92-J-1365), the National Science Foundation (ATM92-96067), and the National Aeronautics and Space Administration (NAG-2-760). We thank Ofer Sneh for help with the CO₂ laser. B.S.B. acknowledges support from a NASA Graduate Student Researchers Fellowship. K.L.F. thanks the David and Lucille Packard Foundation for a graduate fellowship from the Packard Scholars Program. S.M.G. and M.A.T. acknowledge the National Science Foundation for PYI and NYI awards, respectively.

References and Notes

- (1) Solomon, S. *Rev. Geophys.* **1988**, *26*, 131.
- (2) See entire issue, *Geophys. Res. Lett.* **1990**, *17*, 313.
- (3) Molina, M. J.; Tso, T. L.; Molina, L. T.; Wang, F. C. Y. *Science* **1987**, *238*, 1253.
- (4) Tolbert, M. A.; Rossi, M. J.; Malhotra, R.; Golden, D. M. *Science* **1987**, *238*, 1258.
- (5) Leu, M. T. *Geophys. Res. Lett.* **1988**, *15*, 17.
- (6) Moore, S. B.; Keyser, L. F.; Leu, M. T.; Turco, R. P.; Smith, R. H. *Nature* **1990**, *345*, 333.
- (7) Leu, M. T.; Moore, S. B.; Keyser, L. F. *J. Phys. Chem.* **1991**, *95*, 7763.
- (8) Hanson, D. R.; Ravishankara, A. R. *J. Geophys. Res.* **1991**, *96*, 5081.
- (9) Abbatt, J. P. D.; Molina, M. J. *J. Phys. Chem.* **1992**, *96*, 7674.
- (10) Toohy, D. W.; Avallone, L. M.; Lait, L. R.; Newman, P. A.; Schoeberl, M. R.; Fahey, D. W.; Woodbridge, E. L.; Anderson, J. G. *Science* **1993**, *261*, 1134.
- (11) Webster, C. R.; May, R. D.; Toohy, D. W.; Avallone, L. M.; Anderson, J. G.; Newman, P. A.; Lait, L. R.; Schoeberl, M. R.; Elkins, J.; Chan, K. R. *Science* **1993**, *261*, 1130.
- (12) Kawa, S. R.; Fahey, D. W.; Heidt, L. E.; Pollock, W. H.; Solomon, S.; Anderson, D. E.; Loewenstein, M.; Proffitt, M. H.; Margitan, J. J.; Chan, K. R. *J. Geophys. Res.* **1992**, *97*, 7905.
- (13) Rodriguez, J. M.; Ko, M. K. W.; Sze, N. D.; Pierce, S. D.; Anderson, J. G.; Fahey, D. W.; Kelly, K.; Farmer, C. B.; Toon, G. C.; Coffey, M. T.; Heidt, L. E.; Mankin, W. G.; Chan, K. R.; Starr, W. L.; Vedder, J. F.; McCormick, M. P. *J. Geophys. Res.* **1989**, *94*, 16683.
- (14) Solomon, S. *Nature* **1990**, *347*, 6291.
- (15) Brasseur, G. P.; Granier, C.; Walters, S. *Nature* **1990**, *348*, 626.
- (16) Jones, R. L.; McKenna, D. S.; Poole, L. R.; Solomon, S. *Geophys. Res. Lett.* **1990**, *17*, 545.
- (17) Salawitch, R. J.; Wofsy, S. C.; McElroy, M. B. *Geophys. Res. Lett.* **1988**, *15*, 871.
- (18) Prather, M. J. *Nature* **1992**, *355*, 534.
- (19) Turco, R. P.; Toon, O. B.; Hamill, P. J. *Geophys. Res.* **1989**, *94*, 16493.
- (20) Toon, O. B.; Hamill, P.; Turco, R. P.; Pinto, J. *Geophys. Res. Lett.* **1986**, *13*, 1284.
- (21) McElroy, M. B.; Salawitch, R. J.; Wofsy, S. C. *Geophys. Res. Lett.* **1986**, *13*, 1296.
- (22) Crutzen, P. J.; Arnold, F. *Nature* **1986**, *324*, 651.
- (23) Hanson, D.; Mauersberger, K. *Geophys. Res. Lett.* **1988**, *15*, 855.
- (24) Middlebrook, A. M.; Koehler, B. G.; McNeill, L. S.; Tolbert, M. A. *Geophys. Res. Lett.* **1992**, *19*, 2417.
- (25) Worsnop, D. R.; Fox, L. E.; Zahniser, M. S.; Wofsy, S. C. *Science* **1993**, *259*, 71.
- (26) Hanson, D. R. *Geophys. Res. Lett.* **1990**, *17*, 421.
- (27) Hamill, P.; Turco, R. P.; Toon, O. B. *J. Atmos. Chem.* **1988**, *7*, 287.
- (28) Toon, O. B.; Browell, E. V.; Kinne, S.; Jordan, J. *Geophys. Res. Lett.* **1990**, *17*, 393.
- (29) Rosen, J. M.; Kjome, N. T.; Oltmans, S. J. *Geophys. Res. Lett.* **1990**, *17*, 1271.
- (30) Deshler, T.; Adriani, A.; Hofmann, D. J.; Gobbi, G. P. *Geophys. Res. Lett.* **1991**, *18*, 1999.
- (31) Baumgardner, D.; Dye, J. E.; Gandrud, B. W.; Knollenberg, R. G. *J. Geophys. Res.* **1992**, *97*, 8035.
- (32) Tro, N. J.; Haynes, D. R.; Nishimura, A. M.; George, S. M. *J. Chem. Phys.* **1989**, *91*, 5778.
- (33) Tro, N. J.; Nishimura, A. M.; George, S. M. *J. Phys. Chem.* **1989**, *93*, 3276.
- (34) Vandoni, M. R. *Mem. Serv. Chim. Etat (Paris)* **1944**, *31*, 87.
- (35) Ritzhaupt, G.; Devlin, J. P. *J. Phys. Chem.* **1991**, *95*, 90.
- (36) Koehler, B. G.; Middlebrook, A. M.; Tolbert, M. A. *J. Geophys. Res.* **1992**, *97*, 8065.
- (37) Haynes, D. R.; Tro, N. J.; George, S. M. *J. Phys. Chem.* **1992**, *96*, 8502.
- (38) Born, M.; Wolf, E. *Principles of Optics*; Pergamon Press: Oxford, 1975.
- (39) Malitson, I. H. *J. Opt. Soc. Am.* **1962**, *52*, 1377.
- (40) Toon, O. B.; Pollack, J. B.; Khare, B. N. *J. Geophys. Res.* **1976**, *81*, 5733.
- (41) Heavens, O. S. *Optical Properties of Thin Solid Films*; Dover Publications: New York, 1991.
- (42) We note that there is a sign error on p 80 in Heavens' book (ref 41). The equation for q_{13} should be $q_{13} = (1 - g_1g_2 + g_2g_3 - g_3g_1) \sin \gamma_1 \cos \gamma_2 + (1 + g_1g_2 - g_2g_3 - g_3g_1) \sin \gamma_2 \cos \gamma_1$.
- (43) Mak, C. H.; Brand, J. L.; Deckert, A. A.; George, S. M. *J. Chem. Phys.* **1986**, *85*, 1676.
- (44) Hall, R. B.; DeSantolo, A. M. *Surf. Sci.* **1984**, *137*, 421.
- (45) George, S. M. In *Investigations of Surfaces and Interfaces—Part A*; Rossiter, B. W., Boetzold, R. C., Eds.; *Physical Methods of Chemistry Series*, 2nd ed., Vol. IX A; John Wiley and Sons: New York, 1993.
- (46) Arthur, D. A.; Meixner, D. L.; Boudart, M.; George, S. M. *J. Chem. Phys.* **1991**, *95*, 8521.
- (47) Cataliotti, R. *J. Chem. Phys.* **1980**, *72*, 3304.
- (48) Eisenberg, D.; Kauzmann, W. *The Structure and Properties of Water*; Oxford University Press: New York, 1969.
- (49) Toon, O. B.; Tolbert, M. A.; Koehler, B. G.; Middlebrook, A.; Jordan, J., in preparation.
- (50) Deckert, A. A.; Brand, J. L.; Mak, C. H.; Koehler, B. G.; George, S. M. *J. Chem. Phys.* **1987**, *87*, 1936.
- (51) Stern, S. A.; Mullhaupt, J. T.; Kay, W. B. *Chem. Rev.* **1960**, *60*, 185.
- (52) Warren, S. G. *Appl. Opt.* **1984**, *23*, 1206.
- (53) Rowland, B.; Devlin, J. P. *J. Chem. Phys.* **1991**, *94*, 812.
- (54) Mayer, E.; Pletzer, R. *Nature* **1986**, *319*, 298.
- (55) Seiber, B. A.; Wood, B. E.; Smith, A. M.; Muller, P. R. *Science* **1979**, *170*, 652.
- (56) Browell, E. V.; Anderson, R. C. *J. Opt. Soc. Am.* **1975**, *65*, 919.
- (57) Bottcher, C. J. F. *Theory of Electric Polarization*; Elsevier Publishing: Amsterdam, 1952.
- (58) Perry, J. H. *Chemical Engineers' Handbook*; McGraw-Hill: New York, 1941.
- (59) Taesler, I.; Delaplane, G.; Olovsson, I. *Acta Crystallogr.* **1975**, *B31*, 1489.
- (60) Delaplane, R. G.; Taesler, I.; Olovsson, I. *Acta Crystallogr.* **1975**, *B31*, 1486.
- (61) Timmermans, J. *The Physico-chemical Constants of Binary Systems in Concentrated Solutions*; Interscience Publishers: New York, 1960; Vol. 4.
- (62) Molina, M. J.; Zhang, R.; Wooldridge, P. J.; McMahon, J. R.; Kim, J. E.; Chang, H. Y.; Beyer, K. D. *Science* **1993**, *261*, 1418.